Diffuse-interface capturing methods for compressible multiphase fluid flows and elastic-plastic deformation in solids: Part II. Results and discussion

By S. S. Jain, M. C. Adler, J. R. West, A. Mani AND S. K. Lele

1. Motivation and objectives

In this study, we choose the three popular diffuse-interface-capturing methods for compressible two-phase flows, and evaluate their performance by simulating a wide range of flows with multiphase fluids and solids. The first approach is the localized-artificial-diffusivity (LAD) method by Cook (2007), Subramaniam *et al.* (2018), and Adler & Lele (2019) that involves adding diffusion terms to the individual phase mass fraction transport equations and are coupled with the other conservation equations. The second approach is the gradient-form approach that is based on the quasi-conservative method proposed by Shukla *et al.* (2010). In this method the diffusion and sharpening terms (together called regularization terms) are added for the individual phase volume fraction transport equations and are coupled with the other conservation equations (Tiwari *et al.* 2013). The third approach is the divergence-form approach that is based on the fully conservative method proposed by Jain *et al.* (2020). In this method, the diffusion and sharpening terms are added to the individual phase volume fraction transport equations and are coupled with the other conservation equations.

This brief is the second part of the two-part brief series. In the first part of the brief (Adler *et al.* 2020*b*), the three diffuse-interface methods considered in this study, along with their implementation, are described in detail. In this brief, we present the simulation results and evaluate the performance of the methods using classical test cases, such as: (a) advection of an air bubble in water, (b) shock interaction with a helium bubble in air, (c) shock interaction and the collapse of an air bubble in water, and (d) Richtmyer-Meshkov instability of a copper-aluminium interface. The simulation test cases chosen in the present study were carefully selected to assess: (1) the conservation property of the method; (2) the accuracy of the method in maintaining the interface shape; (3) the ability of the method in maintaining constant interface thickness throughout the simulation; and (4) the robustness of the method in handling large density ratios.

Some of these test cases have been extensively studied in the past and have been used to evaluate the performance of various interface-capturing and interface-tracking methods. Many studies look at these test cases to evaluate the performance of the methods in the limit of very fine grid resolution. For example, a typical grid size may be on the order of hundreds of points across the diameter of a single bubble/droplet. However, for the practical application of these methods in the large-scale simulations of engineering interest, where there are thousands of droplets, e.g., in atomization processes, it is rarely affordable to use such fine grids to resolve a single droplet/bubble. Therefore, in this study we examine these methods in the opposite limit of relatively coarse grid resolution. This

limit is more informative of the true performance of these methods for practical applications. All three diffuse-interface capturing methods are implemented in the PadéOps solver (Adler *et al.* 2020*a*) to facilitate fair comparison of the methods with the same underlying numerical methods, thereby eliminating any solver/implementation-related bias in the comparison.

The remainder of this brief is outlined as follows. In Section 2, the simulation results are presented and the performance of the three methods is examined. The concluding remarks are made in Section 3 along with a summary.

2. Results

The first test case (Section 2.1) is the advection of an air bubble in water. This test case is chosen to evaluate the ability of the interface-capturing method to maintain the interface shape for long-time numerical integration and to examine the robustness of the method for high-density-ratio interfaces. It is known that the error in evaluating the interface normal accumulates over time and results in artificial alignment of the interface along the grid (Chiodi & Desjardins 2017; Tiwari *et al.* 2013). This behavior is examined for each of the three methods. The second test case (Section 2.2) is the shock interaction with a helium bubble in air. This test case is chosen to evaluate the ability of the methods to conserve mass, to maintain constant interface thickness throughout the simulation, and to examine the behavior of the under-resolved features captured by the methods. The third test case (Section 2.3) is the shock interaction with an air bubble in water. This test case is chosen to evaluate the robustness of the method to handle strong-shock/high-density-ratio interface interactions. The fourth test case (Section 2.4) is the RMI of a copper–aluminum interface. This test case is chosen to illustrate the applicability of the methods to simulate interfaces between solid materials with strength, to examine the conservation properties of the methods in the limit of high interfacial curvature, to examine the ability of the methods to maintain constant interface thickness, and to assess the behavior of the under-resolved features captured by the methods.

To evaluate the mass-conservation property of a method, the total mass, m_k, of the phase k is calculated as

$$m_k = \int_\Omega \rho_k Y_k dv, \qquad \text{with no sum on repeated } k, \tag{2.1}$$

in which the integral is computed over the computational domain Ω. To evaluate the ability of a method to maintain constant interface thickness, we define a new parameter—the interface-thickness indicator (l)—that measures the maximum interface thickness in the domain as

$$l = \max_{\phi=0.5} \left(\frac{1}{\hat{n} \cdot \vec{\nabla}\phi} \right). \tag{2.2}$$

2.1. *Advection of an air bubble in water*

This section examines the continuous advection of a circular air bubble in water, with both phases initialized with a uniform advection velocity. The problem domain spans ($0 \le x \le 1$; $0 \le y \le 1$), with periodic boundary conditions in both dimensions. The domain is discretized on a uniform Cartesian grid of size $N_x = 100$ and $N_y = 100$. The bubble has a radius of 25/89 and is initially placed at the center of the domain.

The material properties for the water medium used in this test case are $\gamma_1 = 4.4$, $\rho_1 = 1.0$, $p_{\infty 1} = 6 \times 10^3$, $\mu_1 = 0$, and $\sigma_{Y1} = 0$. The material properties for the air

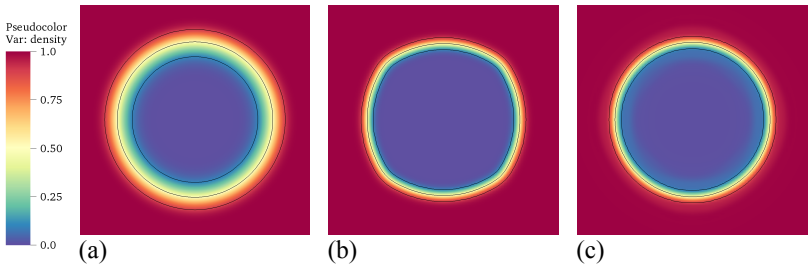

FIGURE 1. Comparison of the final state of the bubble after five flow-through times using (a) LAD approach, (b) divergence-form approach, and (c) gradient-form approach. The three solid black lines denote the isocontours of the volume fraction values of 0.1, 0.5, and 0.9, representing the interface region.

medium used in this test case are $\gamma_2 = 1.4$, $\rho_2 = 1 \times 10^{-3}$, $p_{\infty 2} = 0$, $\mu_2 = 0$, and $\sigma_{Y2} = 0$, where $\gamma_k, \rho_k, p_{\infty k}, \mu_k$, and σ_{Yk} are the ratio of specific heats, density, stiffening pressure, shear modulus, and yield stress of phase k, respectively.

The initial conditions for the velocity, pressure, volume fraction, and density are

$$u = 5, \quad v = 0, \quad p = 1, \quad \phi_1 = \phi_1^\epsilon + (1 - 2\phi_1^\epsilon)\, f_\phi, \quad \phi_2 = 1 - \phi_1, \quad \rho = \phi_1\rho_1 + \phi_2\rho_2, \tag{2.3}$$

respectively, in which the volume fraction function, f_ϕ, is given by

$$f_\phi = \frac{1}{2}\left\{1 - \operatorname{erf}\left[\frac{625/7921 - (x - 1/2)^2 - (y - 1/2)^2}{3\Delta x}\right]\right\}. \tag{2.4}$$

For all the problems, the mass fractions are calculated using the relations $Y_1 = \phi_1\rho_1/\rho$ and $Y_2 = 1 - Y_1$. For this problem, the interface regularization length scale and the out-of-bounds velocity scale are defined by $\epsilon = 1.0 \times 10^{-2}$ and $\Gamma^* = 5.0$, respectively.

The simulation is integrated for a total physical time of $t = 1$ units, and the bubble at this final time is shown in Figure 1, facilitating comparison among the LAD, divergence-form, and gradient-form methods. All three methods perform well and are stable for this high-density-ratio case. The consistent regularization terms included in the momentum and energy equations are necessary to maintain stability. The divergence-form approach results in relatively faster shape distortion compared to the LAD and gradient-form approaches. This shape distortion is due to the accumulation of error resulting from numerical differentiation of the interface normal vector, which is required in the divergence-form approach but not the other approaches. A similar behavior of interface distortion was seen when the velocity was halved and the total time of integration was doubled, thereby confirming that this behavior is reproducible for a given flow-through time (results not shown).

For all the problems in this work, a second-order finite-volume scheme is used for discretization of the interface regularization terms, unless stated otherwise. Two possible ways to mitigate the interface distortion are by refining the grid or by using a higher-order scheme for the interface-regularization terms. Because we are interested in the limit of coarse grid resolution, we study the effect of using an explicit sixth-order finite-difference scheme to discretize the interface regularization terms. As described in Section 2.8 of the first part of this brief series (Adler *et al.* 2020*b*), finite-difference schemes may be used to discretize the interface regularization terms—without resulting in spurious behavior—if the nonlinear interface sharpening and the counteracting diffusion terms

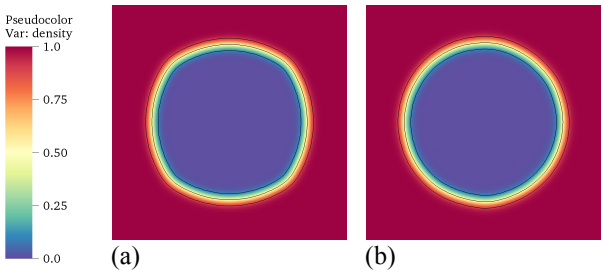

FIGURE 2. Comparison of the state of the bubble after five flow-through times using the divergence-form approach with (a) second-order scheme and (b) sixth-order scheme. The three solid black lines denote the isocontours of the volume fraction values of 0.1, 0.5, and 0.9, representing the interface region.

are formed at the grid faces (staggered locations), from which the derivatives at the grid points (nodes) may be calculated. Comparing the second-order and sixth-order schemes for the interface regularization terms of the divergence-form approach, the final state of the advecting bubble is shown in Figure 2. The interface distortion is significantly reduced using the sixth order scheme.

2.2. *Shock interaction with a helium bubble in air*

This section examines the classic test case of a shock wave traveling through air followed by an interaction with a stationary helium bubble. To examine the interface regularization methods, we model this problem without physical species diffusion; therefore, the interface regularization methods for immiscible phases are applicable, because no physical molecular mixing should be exhibited by the underlying numerical model. The use of immiscible interface-capturing methods to model the interface between the gases in this problem is also motivated by the experiments of Haas & Sturtevant (1987). In these experiments, the authors use a thin plastic membrane to prevent molecular mixing of helium and air.

The problem domain spans $(-2 \leq x \leq 4;\, 0 \leq y \leq 1)$, with periodic boundary conditions in the y direction. A symmetry boundary is applied at $x = 4$, representing a perfectly reflecting wall, and a sponge boundary condition is applied over $(-2 \leq x \leq -1.5)$, modeling a non-reflecting free boundary. The problem is discretized on a uniform Cartesian grid of size $N_x = 600$ and $N_y = 100$. The bubble has a radius of $25/89$ and is initially placed at the location $(x = 0, y = 1/2)$. The material properties for the air medium are described by $\gamma_1 = 1.4$, $\rho_1 = 1.0$, $p_{\infty 1} = 0$, $\mu_1 = 0$, and $\sigma_{Y1} = 0$. The material properties for the helium medium are described by $\gamma_2 = 1.67$, $\rho_2 = 0.138$, $p_{\infty 2} = 0$, $\mu_2 = 0$, and $\sigma_{Y2} = 0$.

The initial conditions for the velocity, pressure, volume fraction, and density are

$$\begin{gathered} u = u^{(2)} f_s + u^{(1)} \left(1 - f_s\right), \quad v = 0, \quad p = p^{(2)} f_s + p^{(1)} \left(1 - f_s\right), \\ \phi_1 = \phi_1^{\epsilon} + \left(1 - 2\phi_1^{\epsilon}\right) f_\phi, \quad \phi_2 = 1 - \phi_1, \quad \rho = \left(\phi_1 \rho_1 + \phi_2 \rho_2\right) \left[\rho^{(2)}/\rho^{(1)} f_s + \left(1 - f_s\right)\right], \end{gathered} \tag{2.5}$$

respectively, in which the volume fraction function, f_ϕ, and the shock function, f_s, are

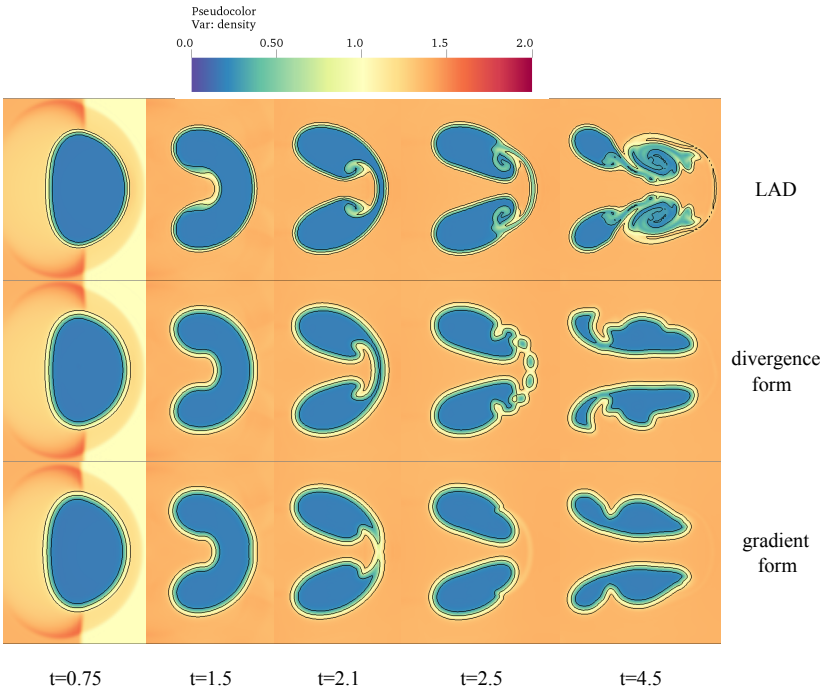

FIGURE 3. Comparison of the bubble shapes at different times for the case of the shock/helium-bubble-in-air interaction using various interface-capturing methods. The three solid black lines denote the isocontours of the volume fraction values of 0.1, 0.5, and 0.9, representing the interface region.

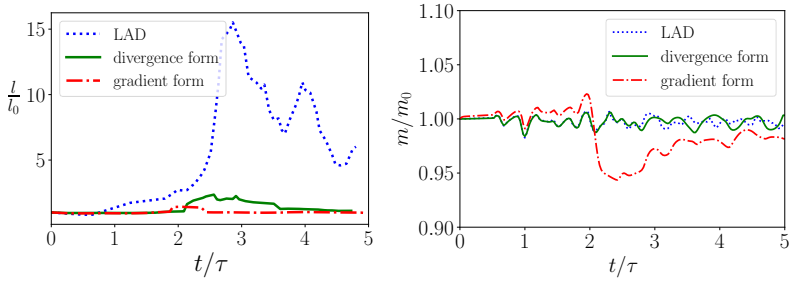

FIGURE 4. (a) Comparison of the interface-thickness indicator, l, by various methods, where l_0 is the maximum interface thickness at time $t = 0$. (b) Comparison of conservation of total mass, m, of the helium bubble by various methods, where m_0 is the mass at time $t = 0$.

given by

$$f_\phi = \frac{1}{2}\left\{1 - \mathrm{erf}\left[\frac{625/7921 - x^2 - (y-1/2)^2}{\Delta x}\right]\right\} \quad \text{and} \quad f_s = \frac{1}{2}\left[1 - \mathrm{erf}\left(\frac{x+1}{2\Delta x}\right)\right], \tag{2.6}$$

respectively, with jump conditions across the shock for velocity $\left(u^{(1)} = 0;\, u^{(2)} = 0.39473\right)$, density $\left(\rho^{(1)} = 1,\ \rho^{(2)} = 1.3764\right)$, and pressure $\left(p^{(1)} = 1;\, p^{(2)} = 1.5698\right)$. For this problem, the interface regularization length scale and the out-of-bounds velocity scale are defined by $\epsilon = 2.5 \times 10^{-2}$ and $\Gamma^* = 2.5$, respectively.

The interaction of the shock with the helium bubble and the eventual breakup of the bubble are shown in Figure 3, with depictions of the evolution at various times, for the LAD, divergence-form, and gradient-form approaches. The bubble can be seen to undergo breakup at an approximate (non-dimensional) time of $t = 2.5$. After this time, the simulation cannot be considered physical because of the under-resolved processes associated with the breakup and the lack of explicit subgrid models for these processes; each interface regularization approach treats the under-resolved processes differently. Therefore, there is no consensus on the final shape of the bubble among the three methods. Yet, a qualitative comparison between the three methods can still be made using the results presented in Figure 3.

Using the LAD approach, the interface diffuses excessively in the regions of high shear, unlike the divergence-form and gradient-form approaches, where the interface thickness is constant throughout the simulation. However, using the LAD approach, the interface remains sharp in the regions where there is no shearing. To quantify the amount of interface diffusion, the interface-thickness indicator [l of Eq. (2.2)] is plotted in Figure 4(a) for the three methods. The thickness indicator (l) increases almost 15 times for the LAD method, whereas it remains on the order of one for the other two methods. This demonstrates a deficiency of the LAD approach for problems that involve significant shearing at an interface that is not subjected to compression.

Furthermore, the behavior of bubble breakup is significantly different among the various methods. Depending on the application, any one of these methods may or may not result in an appropriate representation of the under-resolved processes. However, for the current study that involves modeling interfaces between immiscible fluids, the grid-induced breakup of the divergence-form approach may be more suitable than the diffusion of the fine structures in the LAD approach or the premature loss of fine structures and associated conservation error of the gradient-form approach. For the LAD approach, the thin film formed at around time $t = 2.1$ does not break; rather, it evolves into a thin region of well-mixed fluid. This behavior may be considered unphysical for two immiscible fluids, for which the physical interface is infinitely sharp in a continuum sense; this behavior would be more appropriate for miscible fluids. For the divergence-form approach, the thin film forms satellite bubbles, which is expected when there is a breakage of a thin ligament between droplets or bubbles due to surface-tension effects. However, this breakup may not be considered completely physical without any surface-tension forces, because the breakup is triggered by the lack of grid support. For the gradient-form approach, the thin film formed at around time $t = 2.1$ breaks prematurely and disappears with no formation of satellite bubbles, and the mass of the film is lost to conservation error.

In Figure 2 of Shukla *et al.* (2010), without the use of interface regularization terms, the interface thickness is seen to increase significantly. Their approach without interface regularization terms is most similar to our LAD approach, because the LAD approach does not include any sharpening terms. Therefore, comparing these results suggests that the thickening of the interface in their case was due to the use of the more dissipative Riemann-solver/reconstruction scheme. The results from the gradient-form approach also match well with the results of the similar method shown in Figure 2 of Shukla *et al.* (2010), which further verifies our implementation. Finally, there is no consensus on the final shape of the bubble among the three methods, which is to be expected, because there are no surface-tension forces and the breakup is triggered by the lack of grid resolution.

To further quantify the amount of mass lost or gained, the total mass of the bubble

is computed using Eq. (2.1) and is plotted over time in Figure 4(b). Small variations in the mass of the bubble for the LAD and divergence-form approaches are primarily due to the discrepancy between the high-order operators used in the computation step and the low-order integration operators used in the post-processing step, which otherwise would have constant mass up to machine precision due to the conservative nature of the methods. For the gradient-form approach, the loss of mass is observed to be largest when the bubble is about to break. This is because the mass-conservation error in the gradient-form approach is proportional to the local curvature, as described in Section 2.7 of the first part of this brief series (Adler *et al.* 2020*b*). Therefore, at the onset of breakup, thin film rupture is different from the other two methods, and the satellite bubbles are absent.

2.3. *Shock interaction with an air bubble in water*

This section examines a shock wave traveling through water followed by an interaction with a stationary air bubble. The material properties are the same as those described in Section 2.1.

The initial conditions for the velocity, pressure, volume fraction, and density are

$$\begin{gathered} u = u^{(2)} f_s + u^{(1)} \left(1 - f_s\right), \quad v = 0, \quad p = p^{(2)} f_s + p^{(1)} \left(1 - f_s\right), \\ \phi_1 = \phi_1^{\epsilon} + \left(1 - 2\phi_1^{\epsilon}\right) f_\phi, \quad \phi_2 = 1 - \phi_1, \quad \rho = \left(\phi_1 \rho_1 + \phi_2 \rho_2\right) \left[\rho^{(2)}/\rho^{(1)} f_s + \left(1 - f_s\right)\right], \end{gathered} \tag{2.7}$$

respectively, in which the volume fraction function, f_ϕ, and the shock function, f_s, are given by,

$$f_\phi = \frac{1}{2}\left\{1 - \operatorname{erf}\left[\frac{1 - \left(x - 2.375\right)^2 - \left(y - 2.5\right)^2}{\Delta x}\right]\right\} \quad \text{and} \quad f_s = \frac{1}{2}\left[1 - \operatorname{erf}\left(\frac{x+1}{10\Delta x}\right)\right], \tag{2.8}$$

respectively, with jump conditions across the shock for velocity $\left(u^{(1)} = 0;\, u^{(2)} = 68.5176\right)$, density $\left(\rho^{(1)} = 1,\ \rho^{(2)} = 1.32479\right)$, and pressure $\left(p^{(1)} = 1;\, p^{(2)} = 19150\right)$.

The problem domain spans $(-2 \leq x \leq 8;\, 0 \leq y \leq 5)$, with periodic boundary conditions in the y direction. A symmetry boundary is applied at $x = 8$, representing a perfectly reflecting wall, and a sponge boundary condition is applied over $(-2 \leq x \leq -1.5)$, modeling a non-reflecting free boundary. The problem is discretized on a uniform Cartesian grid of size $N_x = 400$ and $N_y = 200$. A second-order, penta-diagonal, Padé filter is employed for dealiasing in this problem to improve the stability of the shock/bubble interaction. For this problem, the artificial bulk viscosity, artificial thermal conductivity, artificial diffusivity, interface regularization length scale, interface regularization velocity scale, and out-of-bounds velocity scale are defined by $C_\beta = 20$, $C_\kappa = 0.1$, $C_D = 20$, $\epsilon = 2.5 \times 10^{-2}$, $\Gamma = 2.0$, and $\Gamma^* = 0.0$, respectively.

Notably, for this problem, the LAD in the mass equations is also necessarily included in the divergence-form and gradient-form approaches to maintain stability. The latter approaches become unstable for this problem for large Γ (the velocity scale for interface regularization). The reason for this is presently unclear, but may result from excessively fast interface regularization speed relative to sound speed coupled with the pressure-temperature equilibration process; this is the subject of ongoing investigation. Figure 5 describes the evolution in time of the shock/bubble interaction and the subsequent bubble collapse. There is no significant difference between the various regularization methods for this problem. The similarity is due to the short convective timescale of the flow relative to

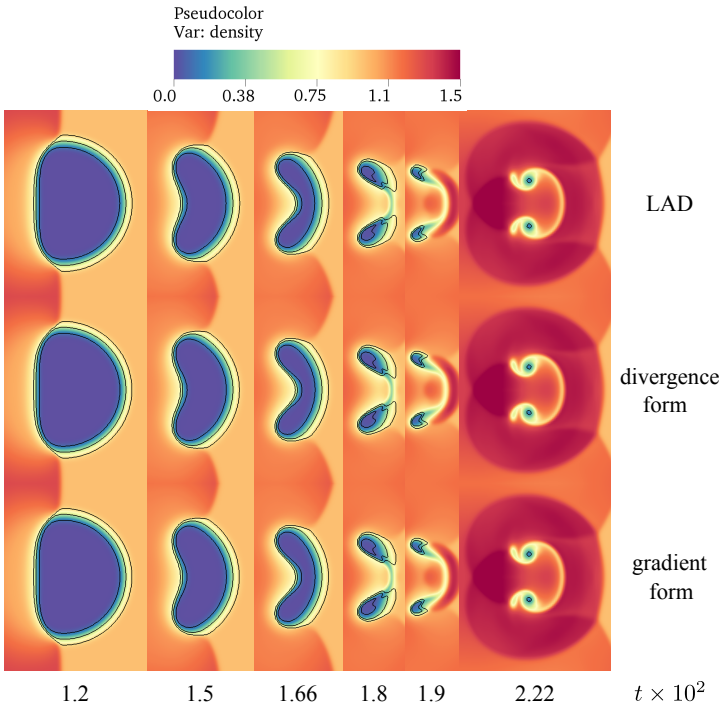

FIGURE 5. Comparison of the bubble shapes at different times for the case of shock/air-bubble-in-water interaction using various interface-capturing methods. The three solid black lines denote the isocontours of the volume fraction values of 0.1, 0.5, and 0.9, representing the interface region.

the maximum stable timescale of the volume fraction regularization methods; effectively, all methods remain qualitatively similar to the LAD approach.

2.4. *Richtmyer–Meshkov instability of a copper–aluminum interface*

This section examines a shock wave traveling through copper followed by an interaction with a sinusoidally distorted copper–aluminum material interface, which has been examined in several previous studies (Lopez Ortega 2013; Subramaniam *et al.* 2018; Adler & Lele 2019). The problem domain spans $(-2 \le x \le 4;\ 0 \le y \le 1)$, with periodic boundary conditions in the y direction. A symmetry boundary is applied at $x = 4$, representing a perfectly reflecting wall, and a sponge boundary condition is applied over $(-2 \le x \le -1.5)$, modeling a non-reflecting free boundary. The problem is discretized on a uniform Cartesian grid of size $N_x = 768$ and $N_y = 128$. The material properties for the copper medium are described by $\gamma_1 = 2.0$, $\rho_1 = 1.0$, $p_{\infty 1} = 1.0$, $\mu_1 = 0.2886$, and $\sigma_{Y1} = 8.79 \times 10^{-4}$. The material properties for the aluminum medium are described by $\gamma_2 = 2.088$, $\rho_2 = 0.3037$, $p_{\infty 2} = 0.5047$, $\mu_2 = 0.1985$, and $\sigma_{Y2} = 2.176 \times 10^{-3}$.

The initial conditions for the velocity, pressure, volume fraction, and density are

$$u = u^{(2)} f_s + u^{(1)} (1 - f_s), \quad v = 0, \quad p = p^{(2)} f_s + p^{(1)} (1 - f_s),$$
$$\phi_1 = \phi_1^{\epsilon} + (1 - 2\phi_1^{\epsilon}) f_\phi, \quad \phi_2 = 1 - \phi_1, \quad \rho = (\phi_1 \rho_1 + \phi_2 \rho_2) \left[\rho^{(2)}/\rho^{(1)} f_s + (1 - f_s)\right], \tag{2.9}$$

respectively, in which the volume fraction function, f_ϕ, and the shock function, f_s, are

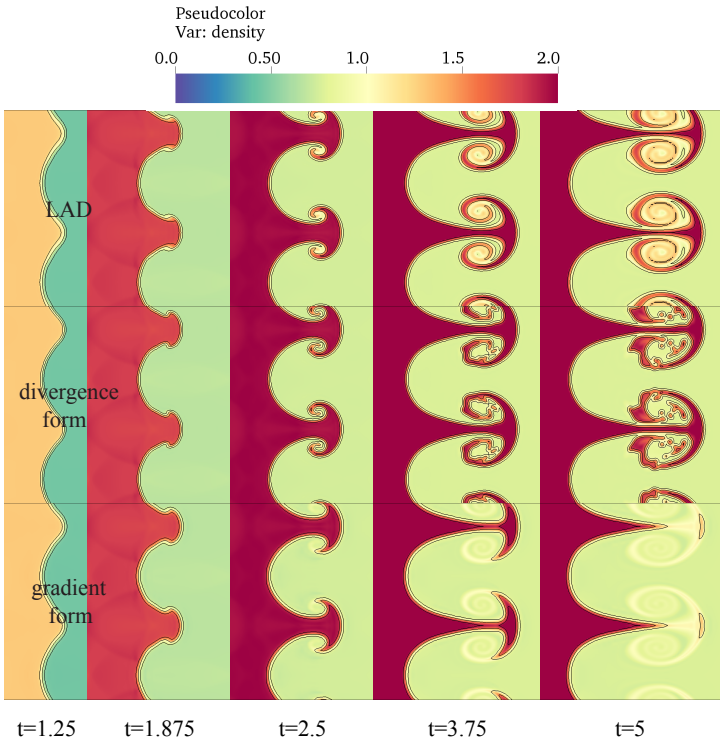

FIGURE 6. Comparison of the copper–aluminum interface shapes at different times for the Cu-Al RMI case using various interface-capturing methods. The three solid black lines denote the isocontours of the volume fraction values of 0.1, 0.5, and 0.9, representing the interface region.

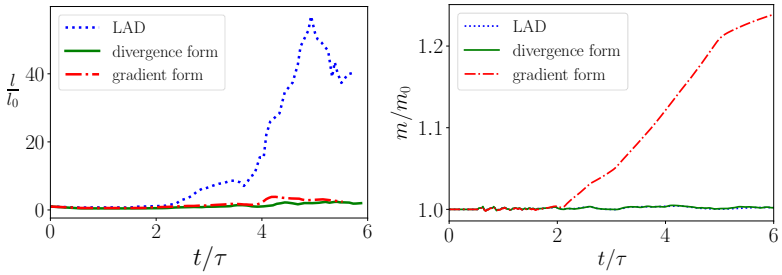

FIGURE 7. (a) Comparison of the interface-thickness indicator, l, by various methods, where l_0 is the maximum interface thickness at time $t = 0$. (b) Comparison of conservation of total mass, m, of aluminum by various methods, where m_0 is the mass at time $t = 0$.

given by

$$f_\phi = \frac{1}{2}\left(1 - \mathrm{erf}\left\{\frac{x - [2 + 0.4/(4\pi y)\sin(4\pi y)]}{3\Delta x}\right\}\right) \quad \text{and} \quad f_s = \frac{1}{2}\left[1 - \mathrm{erf}\left(\frac{x-1}{2\Delta x}\right)\right], \tag{2.10}$$

respectively, with jump conditions across the shock for velocity $\left(u^{(1)} = 0;\, u^{(2)} = 0.68068\right)$, density $\left(\rho^{(1)} = 1,\ \rho^{(2)} = 1.4365\right)$, and pressure $\left(p^{(1)} = 5 \times 10^{-2};\, p^{(2)} = 1.25\right)$. The kinematic tensors are initialized in a pre-strained state consistent with the material compression associated with shock initialization, assuming no plastic deformation has yet

occurred, with

$$g_{ij} = g^e_{ij} = \begin{cases} \left[\rho^{(2)} f_s + \rho^{(1)} \left(1 - f_s\right)\right] / \rho_1, & \text{for } i = j = 1 \\ \delta_{ij}, & \text{else} \end{cases} \qquad \text{and} \qquad g^p_{ij} = \delta_{ij}. \quad (2.11)$$

For this problem, the interface regularization length scale and the out-of-bounds velocity scale are defined by $\epsilon = 3.90625 \times 10^{-3}$ and $\Gamma^* = 1.0$, respectively.

The time evolution of the growth of the interface instability is shown in Figure 6. The simulation is integrated well into the nonlinear regime where the bubble (lighter medium) and the spike (heavier medium) have interpenetrated, forming mushroom-shaped structures with fine ligaments. The qualitative comparison between the methods in this test case is similar to that of the shock-helium-bubble interaction in air. With the LAD approach, the interface thickness increases with time, especially in the regions of high shear at the later stages. However, with the divergence-form and gradient-form approaches, the interface thickness is constant throughout the simulation. This is quantified by plotting the interface-thickness indicator [l of Eq. (2.2)] for each of the three methods in Figure 7(a). The thickness indicator increases almost 50 times for the LAD method, whereas it stays on the order of one for the other two methods, illustrating that the LAD incurs significant artificial diffusion of the interface at later stages in the nonlinear regime.

It is also evident from Figure 6 that the gradient-form approach results in significant copper mass loss, and the dominant mushroom structure formed in the nonlinear regime is completely lost. To quantify the amount of mass lost or gained, the total mass of the aluminum material [Eq. (2.1)] is plotted against time in Figure 7(b). The gradient-form approach results in significant gain in the mass of the aluminum material, up to 20%, at the later stages of the simulation. This makes it practically unsuitable for accurate interface representation in long-time numerical simulations. With the divergence-form approach, the breakup of the ligaments to form metallic droplets is seen in Figure 6.

3. Concluding remarks

This work examines three diffuse-interface-capturing methods and evaluates their performance for the simulation of immiscible compressible multiphase fluid flows and elastic-plastic deformation in solids. The first approach is the localized-artificial-diffusivity (LAD) method of Cook (2007), Subramaniam *et al.* (2018), and Adler & Lele (2019), in which artificial diffusion terms are added to the individual phase mass fraction transport equations and are coupled with the other conservation equations. The second approach is the gradient-form approach that is based on the quasi-conservative method of Shukla *et al.* (2010). In this method, the diffusion and sharpening terms (together called regularization terms) are added to the individual phase volume fraction transport equations and are coupled with the other conservation equations (Tiwari *et al.* 2013). The third approach is the divergence-form approach that is based on the fully conservative method of Jain *et al.* (2020). In this method, the diffusion and sharpening terms are added to the individual phase volume fraction transport equations and are coupled with the other conservation equations. In the present study, all of these interface regularization methods are used in conjunction with a four-equation, multicomponent mixture model, in which pressure and temperature equilibria are assumed among the various phases. However, the latter two interface regularization methods are commonly explored in the context of a five-equation model, in which temperature equilibrium is not assumed. Therefore, prudence should be

Method	Conservation	Sharp interface	Shape distortion	Behavior of under-resolved ligaments and breakup
LAD	Yes	No (interface diffuses in the regions of high shear)	No	Diffusion (phases artificially diffuse as fine-scale features approach unresolved scales)
Divergence form	Yes	Yes	Yes (interface aligns with the grid)	Breakup (phases artificially break up as fine-scale features approach unresolved scales)
Gradient form	No (under-resolved features will be lost)	Yes	No	No conservation (conservation error is introduced as interface curvature is poorly resolved for fine-scale features)

TABLE 1. Summary of the advantages and disadvantages of the three diffuse-interface capturing methods considered in this study: LAD method based on Cook (2007), Subramaniam *et al.* (2018), and Adler & Lele (2019); divergence-form approach based on Jain *et al.* (2020); and the modified gradient-form approach based on Shukla *et al.* (2010) and Tiwari *et al.* (2013). The relative disadvantages of each approach and the different behaviors of under-resolved processes are underlined.

exercised when making direct comparisons of interface regularization behavior between four-equation and five-equation models.

The primary objective of this work is to compare these three methods in terms of their ability to maintain constant interface thickness throughout the simulation; simulate high-density-ratio interfaces; conserve mass, momentum, and energy; and maintain accurate interface shape for long-time integration. Comparison of the different implicit treatments of subgrid phenomena is also of interest. The LAD method has previously been used for simulating material interfaces between solids with strength (Subramaniam *et al.* 2018; Adler & Lele 2019). Here, we introduce consistent corrections in the kinematic equations for the divergence-form and the gradient-form interface regularization approaches to extend these methods to the simulation of interfaces between solids with strength.

We employ several test cases to evaluate the performance of the methods, including (1) advection of an air bubble in water, (2) shock interaction with a helium bubble in air, (3) shock interaction and the collapse of an air bubble in water, and (4) Richtmyer–Meshkov instability of a copper–aluminum interface. For the application of these methods to large-scale simulations of engineering interest, it is rarely practical to use hundreds of grid points to resolve the diameter of a bubble/drop. Therefore, we choose to study the limit of relatively coarse grid resolution, which is more representative of the true performance of these methods.

The performance of the three methods is summarized in Table 1. The LAD and divergence-form approaches conserve mass, momentum, and energy, whereas the gradient-form approach does not. The mass-conservation error increases proportionately with the local interface curvature; therefore, fine interfacial structures will be lost during the simulation. The divergence-form and gradient-form approaches maintain a constant interface thickness throughout the simulation, whereas the interface thickness of the LAD method

increases in regions of high shear due to the lack of interface sharpening terms to counter the artificial diffusion. The LAD and gradient-form approaches maintain the interface shape for a long time compared to the divergence-form approach; however, the interface distortion of the divergence-form approach can be mitigated with the use of appropriately crafted higher-order schemes for the interface regularization terms.

For each method, the behavior of under-resolved ligaments and breakup features is unique. For the LAD approach, thin ligaments that form at the onset of bubble breakup (or in late-stage RMI) diffuse instead of rupturing. For the gradient-form approach, the ligament formation is not captured because of mass-conservation issues, which result in premature loss of these fine-scale features. For the divergence-form approach, the ligaments rupture due to the lack of grid support, acting like artificial surface tension that becomes significant at the grid scale.

For broader applications, the optimal method depends on the objectives of the study. These applications include (1) well-resolved problems, in which differences in the behavior of under-resolved features is not of concern, (2) applications involving interfaces between miscible phases, and (3) applications involving more complex physics, including regimes in which surface tension or molecular diffusion must be explicitly modeled and problems in which phase changes occur. We intend this demonstration of the advantages, disadvantages, and behavior of under-resolved phenomena exhibited by the various methods to be helpful in the selection of an interface regularization method. These results also provide motivation for the development of subgrid models for multiphase flows.

Acknowledgments

M. C. A. and J. R. W. appreciate the sponsorship of the U.S. Department of Energy Lawrence Livermore National Laboratory under contract DE-AC52-07NA27344 (monitor: Dr. A. W. Cook). S. S. J. is supported by a Franklin P. and Caroline M. Johnson Graduate Fellowship.

REFERENCES

Adler, M. C., Jain, S. S., West, J. R., Mani, A., Lele, S. K. *et al.* 2020*a* PadéOps source code. https://github.com/FPAL-Stanford-University/PadeOps.

Adler, M. C., Jain, S. S., West, J. R., Mani, A. & Lele, S. K. 2020*b* Diffuse-interface capturing methods for compressible multiphase fluid flows and elastic-plastic deformation in solids: Part I. Methods. *Annual Research Briefs,* Center for Turbulence Research, Stanford University, pp. 356–341.

Adler, M. C. & Lele, S. K. 2019 Strain-hardening framework for Eulerian simulations of multi-material elasto-plastic deformation. *Annual Research Briefs,* Center for Turbulence Research, Stanford University, pp. 257–271.

Chiodi, R. & Desjardins, O. 2017 A reformulation of the conservative level set reinitialization equation for accurate and robust simulation of complex multiphase flows. *J. Comput. Phys.* **343**, 186–200.

Cook, A. W. 2007 Artificial fluid properties for large-eddy simulation of compressible turbulent mixing. *Phys. Fluids* **19**, 055103.

Haas, J. F. & Sturtevant, B. 1987 Interaction of weak shock waves with cylindrical and spherical gas inhomogeneities. *J. Fluid Mech.* **181**, 41–76.

Jain, S. S., Mani, A. & Moin, P. 2020 A conservative diffuse-interface method for compressible two-phase flows. *J. Comput. Phys.* **418**, 109606.

Lopez Ortega, A. 2013 *Simulation of Richtmyer-Meshkov flows for elastic-plastic solids in planar and converging geometries using an eulerian framework.* Ph.D. thesis, California Institute of Technology.

Shukla, R. K., Pantano, C. & Freund, J. B. 2010 An interface capturing method for the simulation of multi-phase compressible flows. *J. Comput. Phys.* **229**, 7411–7439.

Subramaniam, A., Ghaisas, N. S. & Lele, S. K. 2018 High-order Eulerian simulations of multimaterial elastic–plastic flow. *J. Fluids Eng.* **140**, 050904.

Tiwari, A., Freund, J. B. & Pantano, C. 2013 A diffuse interface model with immiscibility preservation. *J. Comput. Phys.* **252**, 290–309.